High-performance tellurium-free thermoelectric module for moderate temperatures using α-MgAgSb/Mg_2(Si,Sn)

Arthur Wieder[*1,2], Julia Camut[1], Amandine Duparchy[1], Radhika Deshpande[1], Aidan Cowley[2], Eckhard Müller[1,3], and Johannes de Boor[1,4]*

*E-mail: Arthur.Wieder@dlr.de

[1]Institute of Materials Research, German Aerospace Center (DLR), Cologne, D-51147, Germany
[2]European Astronaut Centre, European Space Agency (ESA), Cologne, D-51147, Germany
[3]Justus Liebig University Giessen, Institute of Inorganic and Analytical Chemistry, Giessen, D-35392, Germany
[4]University of Duisburg-Essen, Faculty of Engineering, Institute of Technology for Nanostructures (NST) and CENIDE, Duisburg, D-47057, Germany

Published paper under: https://doi.org/10.1016/j.mtener.2023.101420

Abstract

α-MgAgSb is a promising thermoelectric material with an average figure of merit above unity between room temperature and 573 K, making it attractive for low temperature waste heat recovery or temperature regulation applications. We demonstrate here the first α-MgAgSb/Mg_2(Si,Sn)-based thermoelectric module, where Mg_2(Si,Sn) was chosen as n-type counterpart due to its excellent thermoelectric properties, low weight and abundant and eco-friendly constituents. By using this new material combination, a maximum conversion efficiency of 6.4% and maximum power of 0.68 W were achieved for a temperature difference of 275 K, superior to commercially available (Bi,Te,Sb)-based thermoelectric modules. The Constant Property Model (CPM) was used to check the validity of the measurement results and to identify room for further improvement. The characterization of the prototype shows relatively good match between measurement and calculation for most of the thermoelectric module performance parameters, however, the measured internal electrical resistance is around 10% higher than the predicted values, indicating opportunities for further enhancement.

Graphical abstract

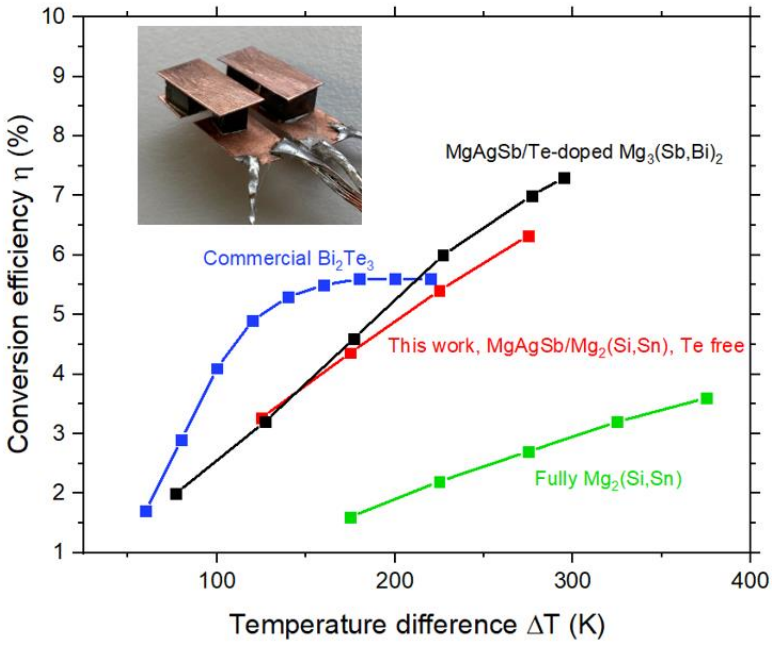

Keywords

Thermoelectricity, Thermoelectric module, Constant Property Model, Conversion efficiency measurement, Power generation

1. Introduction

With energy demand around the world constantly increasing, thermoelectric (TE) materials have attracted great attention in recent years.[1] As more than 60% of the energy generated by burning fossil fuels is dissipated as waste heat, the ability of TE technologies to convert thermal energy directly into electrical energy via the solid state Seebeck effect makes them highly attractive.[2, 3] TE technologies can act as eco-friendly power supply, enhance overall system efficiency and - in combination with other techniques – address the current energy crisis.[4]

The performance of a TE material is gauged by the dimensionless figure of merit $zT = \alpha^2 T/\rho\kappa$, where α is the Seebeck coefficient, T the absolute temperature, ρ the electrical resistivity, and κ the thermal conductivity.[5] Connected electrically in series and thermally in parallel, n-type and p-type thermoelements, called legs, are forming a thermoelectric module (TEM).[6]

The performance of a TEM, if used as thermoelectric generator (TEG), is mainly assessed by its maximum conversion efficiency $\eta_{\max} = \frac{T_\mathrm{h}-T_\mathrm{c}}{T_\mathrm{h}} \frac{\sqrt{1+Z\bar{T}}-1}{\sqrt{1+Z\bar{T}}+\frac{T_\mathrm{c}}{T_\mathrm{h}}}$, where T_h and T_c are the temperatures at hot and cold sides, $\bar{T}$ is the average temperature across the TE legs, and $Z = \frac{(\alpha_\mathrm{p}-\alpha_\mathrm{n})^2}{KR}$ is the figure of merit of a p-n couple with $\alpha_\mathrm{p} - \alpha_\mathrm{n}$ the Seebeck coefficient, K the thermal conductance, and R the resistance.[7]

Although their conversion efficiencies are lower than those of alternative environmentally friendly energy sources, TEMs are competitive due to their exceptional reliability, extended operational lifespan, absence of mechanical components, and minimal maintenance demands.[8, 9] Being used more and more over the years, they have already been demonstrated for several waste heat recovery applications in the fields of steel industry[10], automotive[11], or power plants[12]. The use of thermoelectricity in medical and wearable devices[13], wireless sensor networks[14], or electronic devices[15] was also reported. TE technologies have also been widely used in aerospace applications as Radioisotope Thermoelectric Generators (RTGs) were successfully employed in dozens of NASA and Russian deep space probe (*e.g.* Voyager 1 and 2)[16] and rover (*e.g.* Curiosity)[17] missions over decades in the past, and are the only viable technology to date where power supply from solar cells is not feasible.

The majority of commercially available TEMs are based on bismuth and telluride and Bi_2Te_3 is the most established TE material to date.[18, 19] Hao *et al.*[20] have reported Bi_2Te_3-based TE modules (71 pairs of p-n legs, each leg had a cross-section area of 1.5 x 1.5 mm² and a length of 1.7 mm. N-type legs were provided by Ferrotec Corporation) with conversion efficiencies up to 6.0% for a temperature difference of 217 K, while maximum conversion efficiencies of 7.2% in continuous use between room temperature and 523 K have been reported for TEGs based on Bi_2Te_3 on a laboratory scale.[21] Nevertheless, the utilization of these elements on a larger scale is impeded by factors such as their scarcity (tellurium for instance is available in Earth's crust at less than 0.001 ppm[22]), environmental harm, and toxicity concerns[23]. TEM with attractive conversion

efficiencies have been demonstrated for other performant material families over the last years, such as Half-Heusler compounds (conversion efficiency of 8.3% between 342 and 997 K[24]) or Skutterudites (conversion efficiency of 10.2% between 298 and 872 K[25]). However, these materials can achieve such performances only for high temperatures[26, 27], making them unsuitable for the low- to mid-temperature range. Therefore, the development of high-performance TEMs based on non-scarce and non-toxic elements for the low- to mid-temperature application range is a crucial challenge.

In recent years, the α-phase of MgAgSb has attracted great attention as Kirkham *et al.*[28] identified α-MgAgSb as a suitable and promising p-type TE material. Its constituents (Mg, Ag, Sb) are relatively abundant on earth[29], and the material shows good mechanical properties.[30] Following this discovery, an effective synthesis route was found by Zhao *et al.*[31] The stoichiometry of the material was then fine-tuned by Liu *et al.*[32] and an average figure of merit value zT_{avg} of 1.1 was obtained between room temperature and 573 K. Rodriguez-Barber *et al.* have shown the importance of securing complete reaction of Mg and Ag in the first synthesis step[33] while Duparchy *et al.*[34] have established a comprehensive synthesis-composition-property relationship leading to reproducible results and to one of the highest reported maximum figure of merit value zT_{max} = 1.34 at 561 K. Several reports have attempted to improve the material performance by doping[35, 36] but the effect is usually not dramatic so that nominally undoped material compositions are employed for device making. In this regard, Kraemer *et al*. have demonstrated a high-conversion efficiency of 8.5% for a temperature difference of 225 K for a single leg.[37]

TEMs using α-MgAgSb as p-type TE material have been successfully built recently, using $Mg_3(Sb,Bi)_2$-as n-type counterpart. Liu *et al.* have measured a conversion efficiency of 2.8% at the temperature difference of 95 K[38], while Ying *et al.* have reported a first attempt showing a conversion efficiency of 6.5% for a temperature difference of 250 K.[39] In their newest work, they have obtained a conversion efficiency of 8.5% under a temperature difference of 260 K.[40] While no measured efficiency was reported for an α-MgAgSb/Bi_2Te_3-based TEM, Ouyang and Li have predicted an efficiency of around 10% for a temperature difference of 200 K for a segmented TEM from these materials.[41]

Despite the n-type material cost-effectiveness (≈ $4/kg)[42], lightweight nature (≈ 3 g/cc)[43], and utilization of non-toxic elements, there are currently no studies documenting the assembly of a TEM that integrates p-type α-MgAgSb with n-type $Mg_2(Si,Sn)$. The material shows very good TE properties, as it exhibits a maximum reproducible figure of merit zT_{max} = 1.4 at 723 K around the chemical composition $Mg_2Si_{0.3}Sn_{0.7}$.[43-45] It is considered as one of the best TE materials for the mid temperature range. A few fully $Mg_2(Si,Sn)$-based TEMs were reported in previous published papers: Goyal *et al*. have predicted a maximum efficiency of 5.0% for a temperature difference of 331 K[46] and Camut *et al*. have reported a measured conversion efficiency of 3.6% for an applied temperature difference of 375 K.[47] The performance of such TEMs remains limited mainly because of the p-type $Mg_2(Si,Sn)$ counterpart showing poorer TE properties with a maximum figure of merit zT_{max} = 0.6 at 700 K.[48] Finally, respective coefficients of thermal expansion of both p-type α-MgAgSb (20 x 10^{-6} K^{-1})[32] and n-type $Mg_2(Si,Sn)$ (16-18 x 10^{-6} K^{-1})[49] are relatively close to each other meaning that CTE mismatch exacerbating stress concentration[9] should not impede too much the performance of an α-MgAgSb/$Mg_2(Si,Sn)$-based TEM.

In this work, we demonstrate for the first time an α-MgAgSb/$Mg_2(Si,Sn)$-based-TEM showing competitive performance. We also provide a full characterization of this α-MgAgSb/$Mg_2(Si,Sn)$-based-TEM, including power and conversion efficiency measurement, addressing challenges like

optimization of the materials, interface design, mechanical stability and integrity of the device. To assess the reliability of the measurement and identify room for improvement, comparison with calculations using a Constant Property Model (CPM) is provided. Suggested by Ioffe[50], the model estimates quickly the main TEM performance parameters, such as the open-loop voltage, the open-circuit heat flow, the current and heat flow for maximum power, the internal electrical resistance as well as the power output and the conversion efficiency. Despite the use of several simplifications and assumptions, the CPM allows for quite accurate performance prediction.[51] While the evaluation of the α-MgAgSb/Mg_2(Si,Sn) prototype detailed here exhibits a relatively good concurrence with the values obtained by the CPM for most of the TEM device parameters, the recorded internal electrical resistance surpasses the computed values by approximately 10%, thereby suggesting potential for further improvement.

2. Materials and methods

2.1. Legs fabrication and characterization

Pellets of n-type Mg_2(Si,Sn) solid solution were prepared following the methodology described in previous publications and according to the nominal stoichiometry $Mg_{2.06}Si_{0.3}Sn_{0.665}Bi_{0.035}$.[44, 52] For the p-type α-MgAgSb, pellets were prepared following the synthesis route described by Duparchy *et al.*[34] and according to the nominal stoichiometry $MgAg_{0.97}Sb_{0.995.}$ The n-type Mg_2(Si,Sn) composition contains 3 at.% of excess Mg mainly to compensate for the Mg loss occurring during the material synthesis.

For the functionalized n-type legs, a multilayer contact design was employed: an Al foil (Alfa Aesar, 99.99% purity) directly in contact with the TE pellet and a Cu foil (ChemPUR, 99.995% purity), as represented in figure 2. The Al foils were previously Ar-ion etched and coated on both sides with an 8 µm thick Zn layer acting as an oxidation barrier layer to prevent the formation of a native oxide layer leading to poor contacts.[53] The copper foil, in turn, was introduced to facilitate the soldering process. Indeed, it proved to be more straightforward to solder copper to copper, as opposed to copper to aluminum. As pressure is applied to the pellet during the contacting process, a layer of alumina powder was also employed. Acting as a buffer layer, it reduces the likelihood of crack formation within the pellet. This layer was subsequently removed.

For the p-type counterpart, Ag powder (Alfa Aesar, 99.99% purity) directly in contact with α-MgAgSb powder was used as electrode in a one-step sintering process, as shown in figure 2, similarly to what has been done in previously published papers.[32, 37] After the joining step, the pellets were diced into legs using a Disco DAD321 Automatic Dicing Saw. A cutting speed through the sample of 0.3 mm/s and an angular speed of 30.000 blade rotations per minute were the used settings.

A Potential & Seebeck scanning Microprobe (PSM)[54] was used to measure the specific electrical contact resistance (r_c) between the TE materials and their respective electrodes in order to evaluate the contact quality between both components. Two r_c values were calculated following the methods reported in previous publications.[52, 55] The first method is using the electrical conductivity of the TE material to determine the current density ($r_{c,j(TE)}$), while the second method employs the current passing through the sample as measured on the shunt resistor by the PSM ($r_{c,j(PSM)}$). Figure 1 illustrate these methods. From those, the contact resistances can be obtained from:

$$r_{c,j(TE)} = \frac{(V_{elec} - V_{TE}) * L}{\Delta V_{TE} * \sigma_{TE}} \quad (1)$$

$$r_{\mathrm{c,j(PSM)}} = \frac{(V_{\mathrm{elec}} - V_{\mathrm{TE}}) * A}{I_{\mathrm{PSM}}} \quad (2)$$

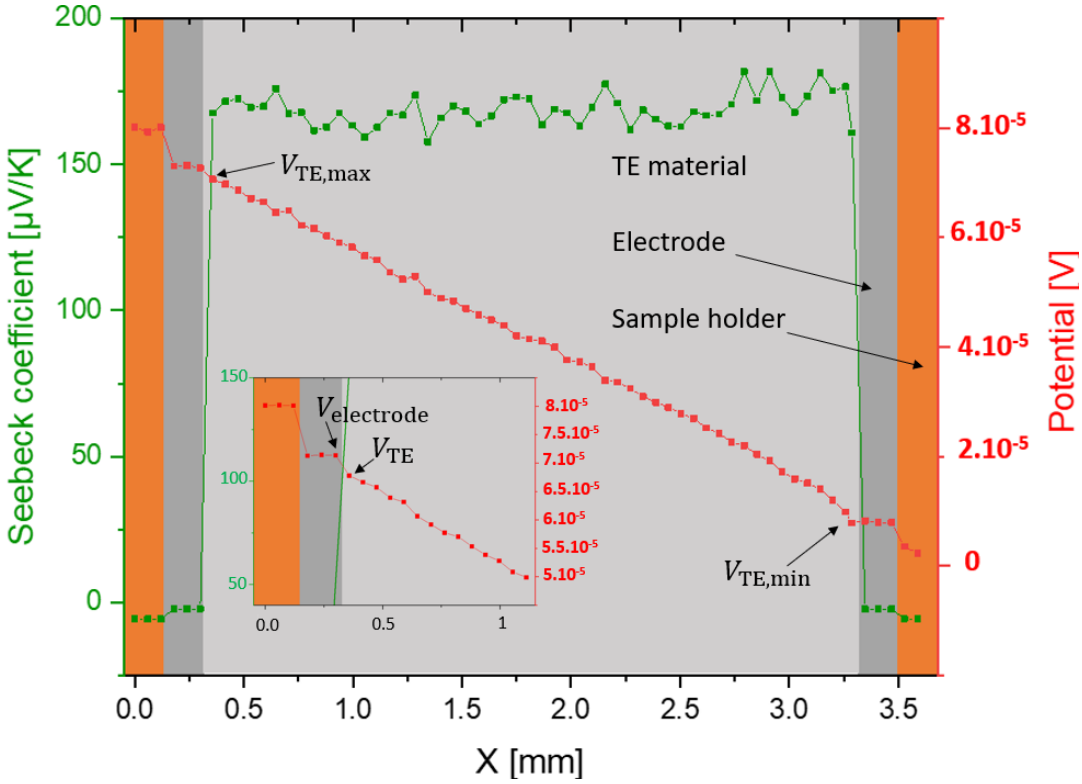

Figure 1: Exemplary line-scan of the Seebeck coefficient and the electrical potential across a contacted p-type leg

$V_{\mathrm{elec}} - V_{\mathrm{TE}}$ is the electrical potential drop at the interface between the TE material and the metallization layer, the position of the interface being itself determined from the abrupt Seebeck coefficient change.[56] L is the length of the TE leg, ΔV_{TE} the electrical potential drop along the TE leg, σ_{TE} the electrical conductivity of the TE material, A the cross-sectional area of the legs, and I_{PSM} the current measured by the PSM. Specific electrical contact resistances of the legs used in the TEM can be found in Table 1.

Leg	n-type		p-type	
Interface	Side 1	Side 2	Side 1	Side 2
$r_{\mathrm{c,j(TE)}}$ (µΩ.cm^2)	17 ± 13	12 ± 8	50 ± 34	42 ± 43
$r_{\mathrm{c,j(PSM)}}$ (µΩ.cm^2)	40 ± 31	28 ± 20	22 ± 14	18 ± 18

Table 1: Average specific electrical contact resistances (and their respective standard deviations) of the legs used inside the TEM

We note that the results from equations (1) and (2) differ by roughly a factor of two and that the order is opposite in n- and p-type materials, respectively. This, as well as the relatively high standard deviations for the contact resistances, indicate some non-uniformity in the contact quality between the TE materials and the metallization layers.[47, 56]

If the material properties are not changing during the contacting step, we can usually assume that $r_{\mathrm{c,j(TE)}}$ gives a more precise value of the specific electrical contact resistance. σ_{TE} at room temperature is known and j_{TE} is obtained using the slope $\Delta V/\Delta x$ inside the TE material for each

line scan individually, allowing to consider irregularities to some extent. As explained further in this report and as outlined in the SI, the amount of material properties change during the contacting step is not significant, and therefore $r_{c,j(TE)}$ values can be considered as reliable. Regarding these values, it can be seen that the specific electrical contact resistance is almost symmetric among both sides of each leg.

By calculating the ratio of contact resistance on both sides of the legs to total leg resistance $n = R_c/(R_c + R_{TE})$, we obtain 16% for the n-type legs, and 10% for the p-type legs. It has been shown in previous published papers that in order for the efficiency not to decrease by more than 20%, the contact electrical resistance should be less than 30% of the total leg resistance for zero thermal contact resistance.[57] A more typical target is n < 10%, indicating limited performance loss in our case due to the electrical contact resistances.

Average values of 15 and 45 μΩ.cm^2 were considered for n-type and p-type legs respectively for the following calculations. The same values were applied either for the hot and cold sides of the legs, in agreement with experimental results for Mg_2Si.[56]

2.2. Module assembly

A TEM was composed of two leg pairs and has been assembled using an induction furnace. To avoid thermal stresses that arise due to the CTE mismatch between the ceramic plate used in standard TEMs and the other components of the TEM[47], the legs were directly connected using copper bridges (250 μm foil, ChemPUR, 99.995% purity) according to an open-design. The TE components were soldered to the copper bridges using 25 μm thick Sn foils (Alfa Aesar, 99.9% purity) and flux paste (Stannol Lötfett soldering grease) was applied on both sides of the foils. The module assembly was performed at 280 °C for 15 minutes with a heating rate of 25 K/min and a load of 6 kg under partial Ar atmosphere. The whole process is summarized in Figure 2.

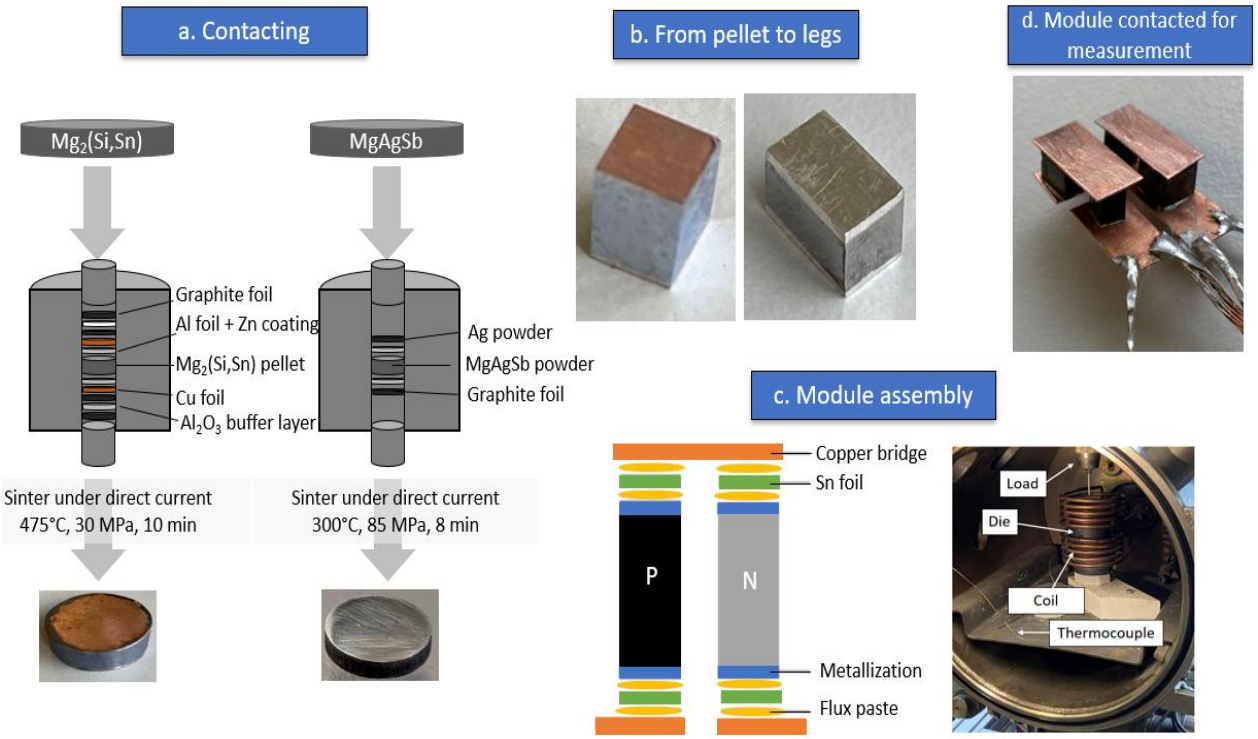

Figure 2: TEM preparation process

The leg geometry is reported in Table 2 and the cross-section ratio was chosen to achieve thermoelectric compatibility between n and p-legs for maximized efficiency as discussed in the SI.[58]

	p-type	n-type
Effective composition	$MgAg_{0.97}Sb_{0.995}$	$Mg_{2.06}Si_{0.3}Sn_{0.665}Bi_{0.035}$
Cross section A (cm^2)	0.6 x 0.4	0.3 x 0.3
TE length L (cm)	0.3	0.3
Average $r_{c,j(TE)}$ (μΩ.cm^2)	45	15

Table 2: Details of the legs used for the TEG assembly

2.3. TEM performance measurement

The Thermoelectric Generator Measurement Apparatus (TEGMA), an in-house developed device, has been used to measure the main TEM performance parameters.[59, 60] Good heat transfer between the different components of the device being a crucial point of the measurement, graphite foils (Dr. Fritsch Gerätebau GmbH, 200 μm thickness) were added between the measured TEM and the components of the measuring section of the device. To avoid an electrical shortcut during the measurement, an insulating ceramic plate has been added on top and bottom of the TEM.

The cold side of the TEM was set at 298 K, and the hot side temperature was varied between 423 and 573 K with a 50 K step. The measurements were performed in vacuum to avoid losses by convection. Note that the hot side temperature of the TE module does not exceed 573 K for two reasons: Firstly, the α phase of MgAgSb transforms into the β phase between 573 and 633 K and into the γ phase for temperatures above 633 K[28], leading to a significant decrease in TE properties. Secondly, while the loss of Mg poses a well-known stability issue in $Mg_2(Si,Sn)$, this effect becomes relevant only for temperatures exceeding approximately 673 K[61], well beyond the temperature range studied here.

Measurement uncertainties for the open-loop voltage, internal electrical resistance, heat flow, conversion efficiency and power output were specified as 0.06% for a measured value of 7.2 V, 2.28% for a measured value of 0.74 Ω, 12% for a measured value of 100 W, 15.7% for a measured value of 4%, and 1.25% for a measured value of 2.5 W, respectively.[59, 60, 62] For the small prototype measured here, heat flow and hence efficiency measurement are suspected to have larger uncertainties, due to *e.g.* the potentially higher impact of radiative heat transfer. Indeed, the accuracy of the in-house measurement set-up was assessed through a comparison with alternative custom-engineered measurement setups in an international round robin initiative.[62]

3. Theory and Evaluation

We employ the CPM using temperature averages (TAv)[50, 63] $\bar{X} = \frac{1}{\Delta T}\int_{T_h}^{T_c} X(T)dT$ to obtain representative averages from the temperature dependent TE properties (α, ρ, and κ) and model the TEM with those.

Despite its simplification[64, 65], predictions of power and efficiency with errors < 2% for $Mg_2(Si,Sn)$[66] have been obtained, which is sufficient for our analysis. As outlined in the SI, for α-

MgAgSb, an error < 1% was obtained in comparison to a 1D solution of the thermoelectric heat balance equation, taking the temperature dependence of the materials into account.

The TE properties of α-MgAgSb and $Mg_2(Si,Sn)$ are shown in figure 3. We obtained an average figure of merit value $zT_{avg} = 1.1$ between room temperature and 573 K consistent with the data found in the literature.[32] Its n-type $Mg_{2.06}Si_{0.3}Sn_{0.665}Bi_{0.035}$ counterpart shows an average figure of merit value $zT_{avg} = 0.7$ between room temperature and 573 K, in the range of the data used in previous published papers[47]. Note that the figure of merit for $Mg_{2.06}Si_{0.3}Sn_{0.665}Bi_{0.035}$ is peaking at 723 K, beyond the temperature interval studied here.[44] The different temperature-dependences between both materials are mainly due to the smaller band gap of MgAgSb.

A figure of merit uncertainty of 14% has to be considered as Seebeck and electrical conductivity measurement are showing an uncertainty of 5%[67], whereas an uncertainty of about 8% is reported for the thermal conductivity.[68]

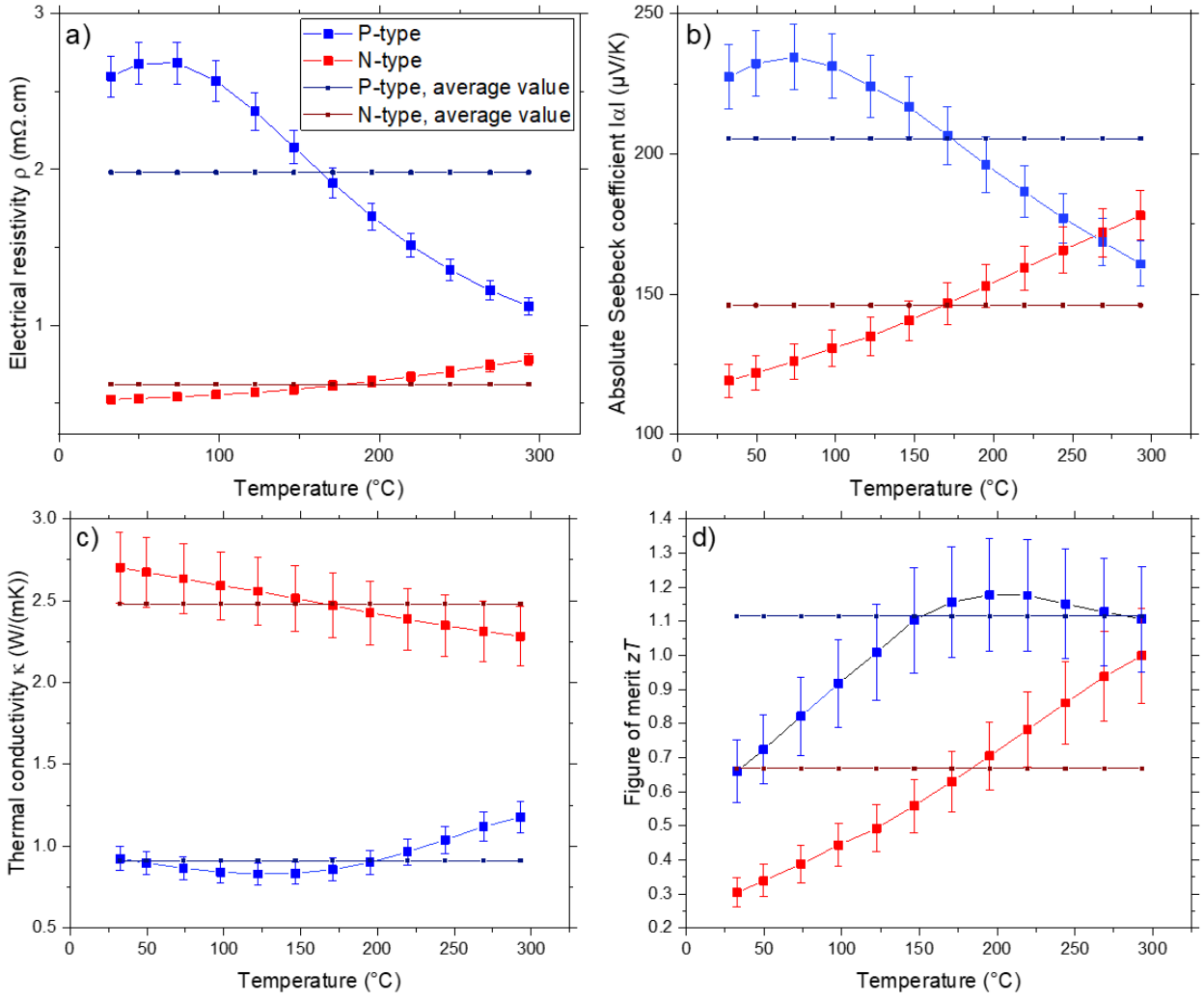

Figure 3: Measured properties over temperature of α-$MgAg_{0.97}Sb_{0.995}$ (p-type, blue) and $Mg_{2.06}Si_{0.3}Sn_{0.665}Bi_{0.035}$ (n-type, red): a) Electrical resistivity, b) Absolute Seebeck coefficient, c) Thermal conductivity, and d) Figure of merit. The legend applies in a) also applies for b), c), and d). Temperature averages of each property for temperatures at the TE legs are given, for a hot side temperature of 300°C and a cold side temperature of 25 °C

The data shown here is representative of the n-type material before contacting. It has been contacted with an Zn-coated Al layer and it has been observed that Zn diffuses in the TE material inducing a gradient in carrier concentration, and therefore in Seebeck coefficient.[47, 53] This inhomogeneity was considered by experimental profiling of the Seebeck coefficient and capturing the corresponding changes in the other thermoelectric properties using a Single Parabolic Band model (SPB).[69] The adapted CPM for inhomogeneous materials (CPIM) is described in detail by Camut *et al.*[70] while the results for the considered case are discussed in the SI where it is shown that the impact is insignificant.

CPM calculations can be performed only if the effective temperatures at the TE legs at the hot and cold sides *i.e.* $T_{\mathrm{TE,h}}$ and $T_{\mathrm{TE,c}}$ are determined. Following the methodology described by Camut *et al.*,[47] these temperatures are determined using the following equations:

$$\Delta T_{\mathrm{TE},0} = \frac{V_{\mathrm{m},0}}{N(\alpha_{\mathrm{p}} - \alpha_{\mathrm{n}})} \tag{3}$$

$$T_{\mathrm{TE,h},0} = T_{\mathrm{m,h},0} - 0.5 * \left(\Delta T_{\mathrm{m},0} - \Delta T_{\mathrm{TE},0}\right) \tag{4}$$

$$T_{\mathrm{TE,c},0} = T_{\mathrm{m,c},0} + 0.5 * \left(\Delta T_{\mathrm{m},0} - \Delta T_{\mathrm{TE},0}\right) \tag{5}$$

where $V_{\mathrm{m},0}$ is the measured open-loop voltage, N the number of unicouples, α_{p} and α_{n} the average Seebeck coefficient values of the p- and n-type legs, respectively, $T_{\mathrm{m,h}}$ the measured hot side temperature at the interface between the TEM and the heater, and $T_{\mathrm{m,c}}$ the measured cold side temperature at the interface between the TEM and the heat flow meter (HFM) ("0" referring to open-loop conditions). Indeed, the measuring section of the facility consists from the top to the bottom of a heater, a geometrical adaptor, the measured TEM, a heat flow meter, and a cooling plate as shown in figure 4, and various temperatures exist between these different components. As represented in figure 4, $\Delta T_{\mathrm{m}} = T_{\mathrm{h,m}} - T_{\mathrm{c,m}}$ is the temperature difference between the edges of the cooling and heating blocks, $\Delta T_{\mathrm{TEM}} = T_{\mathrm{h,TEM}} - T_{\mathrm{c,TEM}}$ is the temperature difference across the TEM, $\Delta T_{\mathrm{TE}} = T_{\mathrm{h,TE}} - T_{\mathrm{c,TE}}$ is the temperature difference across the TE legs, $\Delta T_{\mathrm{par,c}} = T_{\mathrm{c,m}} - T_{\mathrm{c,TE}}$ is the parasitic temperature drop lost at the cold side and $\Delta T_{\mathrm{par,h}} = T_{\mathrm{h,m}} - T_{\mathrm{h,TE}}$ is the parasitic temperature drop lost at the hot side.

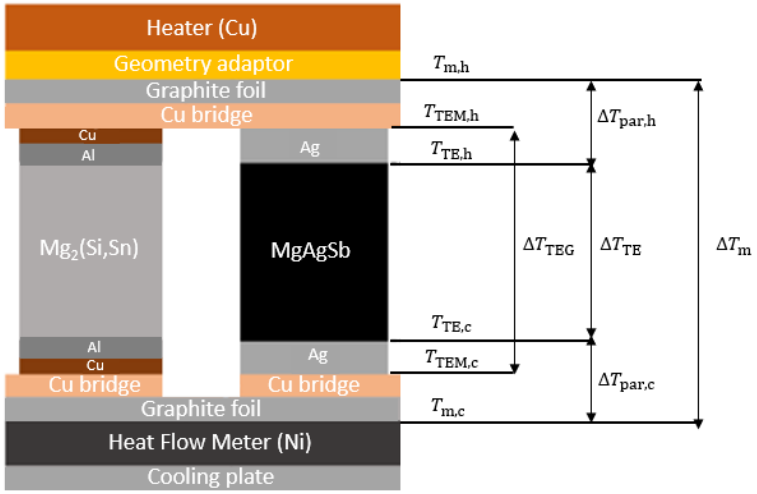

Figure 4: Schematics of the elements and corresponding temperatures of the measurement column surrounding the TEM

As explained by Camut *et al.,*[47] most parameters are relevant for $I \neq 0$, and therefore new effective temperatures at the TE legs for optimum current (according to maximum power output) have to be determined using the following equation:

$$\frac{\dot{Q}_{\mathrm{m,opt}}}{\dot{Q}_{\mathrm{m,0}}} = \frac{\Delta T_{\mathrm{par,opt}}}{\Delta T_{\mathrm{par,0}}} = \frac{\Delta T_{\mathrm{m,opt}} - \Delta T_{\mathrm{TE,opt}}}{\Delta T_{\mathrm{par,0}}} \tag{6}$$

where $\dot{Q}_{\mathrm{m}}$ is the heat flow into the module, and ΔT_{par} the parasitic temperature difference between TE material and the surface of the adjacent heat flow meters or heat exchangers in the measurement; the subscript "opt" referring to optimum current for maximum power output. $\dot{Q}_{\mathrm{m}}$, either for I = 0 or $I = I_{\mathrm{opt}}$, is not directly measured by the TEGMA but obtained from summing the measured power output $P_{\mathrm{m,el}}$ and the measured value of the heat flow at the cold side $\dot{Q}_{\mathrm{m,out}}$, as the HFM has been placed at the cold side of the module only. From equation (6), $\Delta T_{\mathrm{TE,opt}}$ is calculated, and hence $T_{\mathrm{TE,h,opt}}$ and $T_{\mathrm{TE,c,opt}}$ are determined using equations (4) and (5) for $I = I_{\mathrm{opt}}$. It should be specified that equation (6) holds only if the heat flow is constant along the measuring column section. Due to the obtained electrical power $\dot{Q}_{\mathrm{in,opt}} > \dot{Q}_{\mathrm{out,opt}}$, however, the relatively low conversion efficiencies of TEMs allow us to approximate $\dot{Q}_{\mathrm{in,opt}} \approx \dot{Q}_{\mathrm{out,opt}}$ for the calculation of the temperature shift due to the increased thermal conductance of the TEM under current flow.

Knowing the effective temperatures at the TE legs, CPM calculations can be performed and most of TEM relevant performance parameters can be determined. The heat flow at current for maximum power output $\dot{Q}_{\mathrm{opt}}$ is calculated such as:

$$\dot{Q}_{\mathrm{opt}} = K_{\mathrm{TE}}\, \Delta T_{\mathrm{TE,opt}} + I_{\mathrm{opt}}\, N\, (\alpha_{\mathrm{p}} - \alpha_{\mathrm{n}}) T_{\mathrm{TE,h,opt}} - \frac{1}{2} I_{\mathrm{opt}}^2 R \tag{7}$$

where K_{TE} is the thermal conductance of the TE legs, I_{opt} the current for maximum power output and R the internal electrical resistance. The latter is the sum of three contributions: the resistance of the TE legs R_{TE}, the electrical contact resistance between the legs and their electrodes R_{c}, and the resistance of the copper bridges R_{Cu}. These parameters are calculated using the following equations:

$$K_{\mathrm{TE}} = N \left(\frac{\kappa_{\mathrm{p}} A_{\mathrm{p}}}{L} + \frac{\kappa_{\mathrm{n}} A_{\mathrm{n}}}{L} \right) \tag{8}$$

$$I_{\mathrm{opt}} = \frac{N(\alpha_{\mathrm{p}} - \alpha_{\mathrm{n}}) \Delta T_{\mathrm{TE,opt}}}{2R} \tag{9}$$

$$R = R_{\mathrm{TE}} + R_{\mathrm{c}} + R_{\mathrm{Cu}} = N \left[\frac{\rho_{\mathrm{p}} L}{A_{\mathrm{p}}} + \frac{\rho_{\mathrm{n}} L}{A_{\mathrm{n}}} + 2 \left(\frac{r_{\mathrm{c,p}}}{A_{\mathrm{p}}} + \frac{r_{\mathrm{c,n}}}{A_{\mathrm{n}}} \right) \right] + \sum_{\mathrm{i}} \frac{L_{\mathrm{i}}}{\sigma_{\mathrm{Cu}}(T) A_{\mathrm{i}}} \tag{10}$$

Our TEM is composed of two copper plates at the hot side, and three copper plates at the cold side: one plate inside the module and two plates to attach the current leads to the outside. Each copper bridge portion i has an electrical resistance $R_{\mathrm{Cu,i}} = \frac{L_{\mathrm{i}}}{\sigma_{\mathrm{Cu}}(T) A_{\mathrm{i}}}$. The copper has a temperature-dependent electrical conductivity $\sigma_{\mathrm{Cu}}(T)$.[71] Each portion of bridge has a length L_{i} and a cross-section A_{i}. The length was taken from the middle of a leg to the middle of another leg. The resistances of the metallic layers Al, Cu, and Ag between the TE material and the Cu bridge are not considered separately but included in the experimental r_{c} measured by the PSM and the modelled R_{c} in equation (10), respectively.

The open-loop heat flow $\dot{Q}_0$ is calculated by applying equation (7) for I = 0, using $\Delta T_{\mathrm{TE},0}$, $T_{\mathrm{h,TE},0}$, and K_{TE} calculated for open-loop temperature conditions.

Finally, maximum power $P_{\mathrm{el,max}}$ and maximum conversion efficiency η_{max} are calculated using:

$$P_{\mathrm{el,max}} = N\left(P_{\mathrm{el,n}} + P_{\mathrm{el,p}}\right) = \frac{(N(\alpha_{\mathrm{p}}-\alpha_{\mathrm{n}})\Delta T_{\mathrm{TE,opt}})^2}{4R} \tag{11}$$

$$\eta_{\mathrm{max}} = \frac{T_{\mathrm{TE,h,opt}}-T_{\mathrm{TE,c,opt}}}{T_{\mathrm{TE,h,opt}}} \frac{\sqrt{1+ZT_{\mathrm{m}}}-1}{\frac{T_{\mathrm{TE,c,opt}}}{T_{\mathrm{TE,h,opt}}}+\sqrt{1+ZT_{\mathrm{m}}}} \tag{12}$$

$$T_{\mathrm{m}} = \frac{T_{\mathrm{TE,c,opt}}+T_{\mathrm{TE,h,opt}}}{2} \tag{13}$$

$$Z = \frac{N^2(\alpha_{\mathrm{p}}-\alpha_{\mathrm{n}})^2}{K_{\mathrm{TE}}R} \tag{14}$$

In the limit of ideal thermal coupling between the TEM and the heat reservoir, optimum current values for maximum power and efficiency differ by a factor of $\frac{1+\sqrt{1+ZT_{\mathrm{m}}}}{2}$, so they cannot be achieved at the same time. Note that for finite thermal coupling, the value depends on the ratio of the thermal interface resistance and the thermal resistance of the TEM.[72]

4. Results

The results of the three measurement cycles for the open-loop voltage $V_{\mathrm{m},0}$ are shown in figure 5a. The data report a significant increase of 5.8% between the start of the first heating step and the end of the first cooling step, followed by a more stable behaviour during the next cycles (≤ 1%). According to equation (3), an increased open-loop voltage can potentially be explained by either a higher Seebeck coefficient or a higher temperature difference at the TE legs. Several mechanisms can therefore be involved: (i) material changes leading to increased Seebeck coefficient values, (ii) improved thermal coupling between the TEM and the TEGMA leading to increased temperature difference across the TE legs, or (iii) the formation and the propagation of cracks inside the TE legs or at the interfaces resulting in an increase of the temperature difference across the TE legs.

Figure 5b shows the ratio $\Delta T_{\mathrm{TE}}/\Delta T_{\mathrm{m}}$ over the hot side temperature at the TE legs $T_{\mathrm{h,TE}}$. The small variation of $\Delta T_{\mathrm{TE}}/\Delta T_{\mathrm{m}}$ with temperature is not the consequence of a non-reached thermal equilibrium, but rather due to different temperature dependences of the involved thermal resistances. Unlike discussed in [47], there is no obvious evidence of material change as the relative temperature drop over the TE material is relatively constant with temperature and does not exceed 100% . A strong increase to unphysical values can be caused by an increasing Seebeck coefficient during the measurement that is not accounted for when calculating the temperatures. As discussed in the SI, post-measurement Seebeck coefficient values of both n- and p-type legs are not showing any drastic changes. Therefore, the increased open-loop voltage cannot be explained by material change.

As we can see in figure 5b, the relative temperature difference changes mostly during heating. As the relative temperature difference increases, one could deduce that the coupling improves. On the other hand, a step between end of heating and start of cooling is observed. As the material input is not changing, one can conclude that the coupling continued to improve during the holding time between heating and cooling.

Study of heat flow stability is also relevant as coupling quality is mainly governed by the thermal transfer occurring in the TEM and the TEGMA components. figure 5c shows heat flow $\dot{Q}$ (for open-loop and optimum current for maximum power output conditions) versus $T_{\mathrm{h,TE}}$. In both cases the heat flow seems relatively stable over the three cycles, as changes $\leq$ 1.5% are observed. A slightly higher change of 1.8% can be identified at open-loop conditions at the highest temperature during the first cycle, but is probably the consequence of the measurement uncertainty. From stable measured heat flow, one might therefore infer that coupling quality is not improved, which is not in line with the observations in figure 5b.

Figure 5d shows the internal electrical resistance R over $T_{\mathrm{h,TE}}$. A significant increase of 15% is observed between the start of the first heating step and the end of the first cooling step. On a first glance, the first heating measurement can seem a bit surprising: initially the measured values are lower than calculated values and the internal electrical resistance increases with temperature during the first heating, in contrast to the observed decrease with temperature during the second and the third cycles. Indeed, although the resistance of the n-type material increases with temperature, the overall internal electrical resistance decreases with temperature due to the strong decrease of the resistivity of α-MgAgSb above 400 K. During the second and third cycles, the internal electrical resistance is stable, as absolute deviations $\leq$ 1.5% are observed.

In view of such an increase, the formation and the propagation of a large crack might be suspected. However, usually cracking happens suddenly, and thus we should see a step, rather than the observed change seems continuous. Additionally, if cracks are present they do not progress as the third cooling data is showing lower resistance values than the third heating data. Another peculiar feature is that we do not see a decrease in heat flow as would be expected in consequence of crack formation. A plausible explanation of the observed TEM parameter changes can be derived from a combination of different effects: (Micro-) cracks between the TE material and the contacts or inside the TE material might have formed during the measurement. This increased the internal electrical resistance and suppressed heat flow. At the same time the thermal coupling of the module with the measurement system improved, due to a change of the graphite foil or a reduction of one or several of the thermal interface resistances. Whatever the reasons involved, the enhanced thermal coupling led to an increased temperature difference as observed but also to an increased heat flow. The reduced heat flow due to interface properties degradation and increased heat flow due to thermal coupling enhancement compensated each other and led to a stable behaviour as we can see in figure 5c.

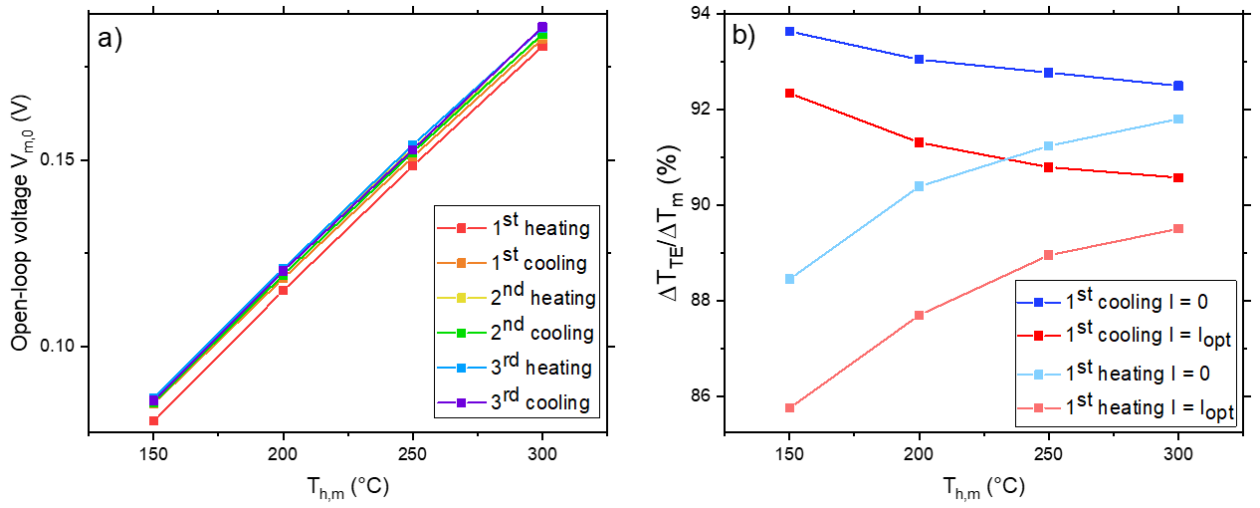

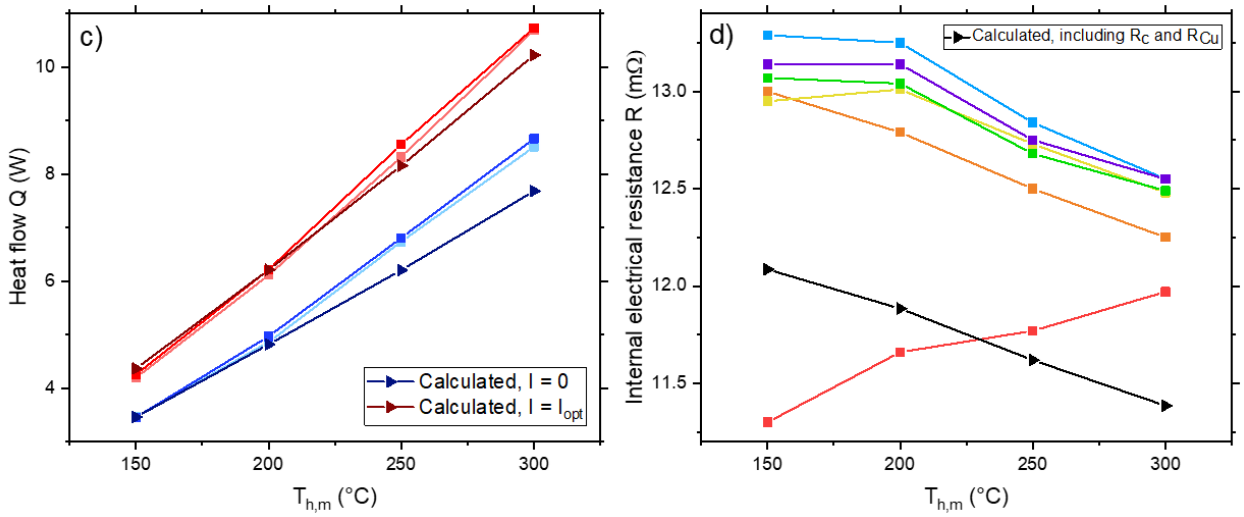

Figure 5: a) Three-cycles measurement of the open-circuit voltage, b) Ratio of the temperature differences across the TE legs and across the TE module for I = 0 and I = I_{opt} during the first-cycle measurement, *c) measurement and calculations of heat flow for I = 0 and I = I_{opt}, for the first measurement cycle, and d) three-cycles measurement and calculations of the internal electrical resistance. The legend of the measured values indicated in a) is also applied in d), and the legend of the measured values indicated in b) is also applied in c)*

Measurement and CPM predictions of the maximum power $P_{\mathrm{el,max}}$ and the maximum conversion efficiency η_{max} are shown in figure 6. A maximum power value of 0.68 W and a maximum conversion efficiency value of 6.4% are reported. $P_{\mathrm{el,max}}$ is stable within 0.5% over the cycles. The stability of the power is explained by the increase of the open-loop voltage and the internal electrical resistance, both values compensating each other. The conversion efficiency data shows some scatter but is also stable.

It can be seen that measured values show a very good agreement with calculated values (black curve in figure 6a) for $P_{\mathrm{el,max}}$. However, a deviation of 7.5% is reported for η_{max}, mainly due to the lower heat flow, and to the measurement uncertainty.

Indeed, in figure 5c, it can be seen that the measured heat flow values are higher than the calculated values (differences of 10 and 5% for $\dot{Q}_0$ and $\dot{Q}_{\mathrm{opt}}$ respectively). The efficiency being inversely proportional to the heat flow, an overestimated heat flow value leads to an underestimated conversion efficiency value. It is therefore not surprising to see conversion efficiency measured values lower than calculated ones. A plausible explanation is a thermal bypass through radiative coupling from the hot side of the TEGMA into the heat flow meter at the cold side. This is suppressed experimentally by using insulating wool around the TEM but cannot be avoided completely and the impact is expected to be larger for small prototypes with low filling factors. Analysis and correction of this has been attempted *e.g.* in [47] and [73] but suffers from uncertainties due to unknown view factors and emissivities.

As we can see in figure 5d, internal electrical resistance measured values are systematically higher than calculated values, except for the first heating measurement. Compared to the predicted values, a maximum deviation of around 10% is observed. This difference can potentially be explained by additional resistances that are not considered in the model (constriction resistance at the contacts, (interface) resistance due to the solder) or additional resistances due to changes

of the module, *e.g.* degradation of the interface between TE material and electrode or microcracks within the TE material. As explained previously, the observed slow and continuous increase in resistance during the first heating is peculiar and not typical for large crack formation, where usually sudden changes are observed.

Within the CPM is it possible to ascribe all additional resistances to effective contact resistances for the n-type legs $r_{c,m,n}$ using:

$$r_{c,m,n} = \frac{(R_m - R_{legs} - R_{Cu})A_n}{2N(1+3*\frac{A_n}{A_p})} \quad (15)$$

We calculated the new n-type effective contact resistances from the cooling data to be around 24 µΩ.cm^2. Before the thermal measurement, specific electrical contact resistance values for both n- and p-type legs differed by a factor of 3. If one considers that the ratio remains constant, the increase in r_c is ascribed to both types of legs proportionally, and therefore one can deduce that $r_{c,m,p} = 3r_{c,m,n}$. As outlined in the SI, using the methodology in [47], detailed calculations are performed, and it can be seen that the previous assumption is valid.

Using these new values, the deviation between measured and calculated conversion efficiency values decreases to a maximum deviation of 3.5% (gray curve in figure 6b). The remaining deviation is due to the differences in measured and calculated heat flow.

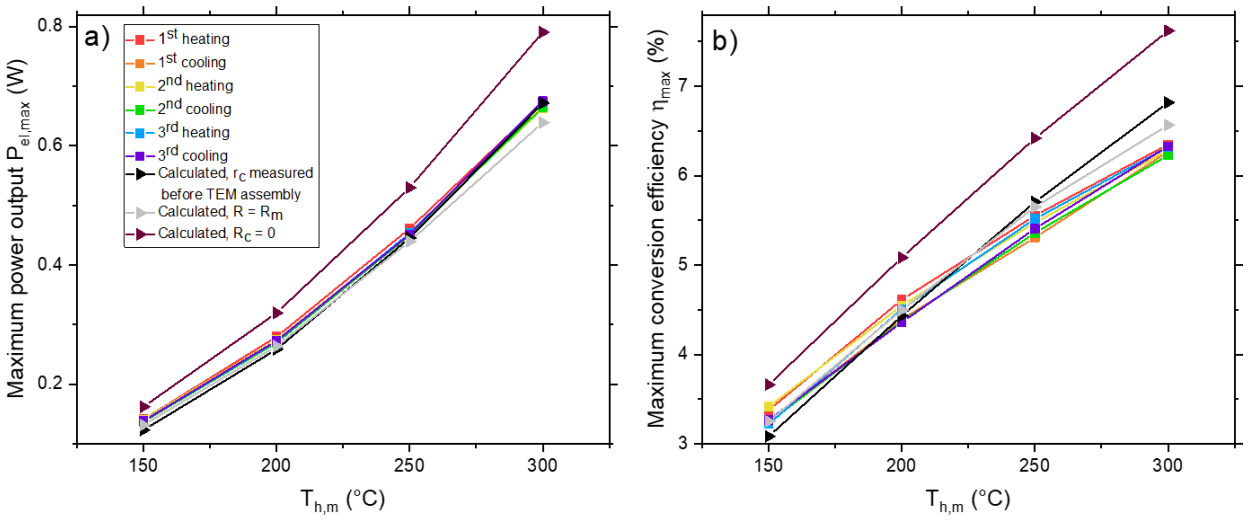

Figure 6: Comparison between measurement and CPM predictions for zero electrical contact resistance, r_c as measured before TEM assembly and effective contact resistance deduced from equation 15 for a) maximum power and b) maximum conversion efficiency. The legend in a) also applies to b).

5. Discussion

The behaviour of the TEM during its measurement can possibly be explained by the combination of several factors: improved thermal coupling is generally expected for modules under characterization, and microcracks leading to additional electrical resistance are not uncommon and widely reported in the literature, especially for $Mg_2(Si,Sn)$-based TEM.[47, 74-76]

Finite Element Method (FEM) analysis would be a suitable tool to identify any mechanical and/or thermal stresses and predict if formation and propagation of cracks are plausible.[77] The

use of thermal imaging during thermal cycling[78] or acoustic techniques[79] to identify mechanical degradation can also be considered.

The reduction of the electrical contact resistance between the TE material and the metallization layer is another challenge that we systematically have to address when building a TEM. In figure 6, calculated maximum power and conversion efficiency for a zero electrical contact resistance are shown. Maximum values of 0.8 W and 7.6% respectively are obtained, corresponding to a 20% deviation from our measured values showing potential for improvement if the contact resistance can be reduced. Achieving better contacts between the TE materials and their respective electrodes is therefore a key issue. Although zero electrical contact resistance is not accessible, lower values than here are possible, as Camut *et al.*[47] have obtained r_c values of 5 μΩ.cm^2 for $Mg_2(Si,Sn)$ n-type legs whereas Ying *et al*.[40] have reported r_c values of 6 μΩ.cm^2 for α-MgAgSb p-type legs.

Furthermore, as the module characterisation was performed at relatively low temperatures, further performance improvement can be expected if $Mg_2(Si,Sn)$ is optimized for low temperature application, possibly by reducing the charge carrier density, as optimum carrier concentration generally decreases with decreasing application temperature.[80]

As this is the first reported α-MgAgSb/$Mg_2(Si,Sn)$ module prototype, there are no direct reference data available. Meaningful comparison can be made with (Bi,Te,Sb)-based modules as a commercially available reference, furthermore with fully $Mg_2(Si,Sn)$-based modules and other combinations with α-MgAgSb, *e.g.* α-MgAgSb/Mg_3Sb_2-based modules. Traditional comparison metric is the geometry independent conversion efficiency.

Figure 7 shows the maximum conversion efficiency of TEMs reported in literature for the low-to-mid temperature application range. It can be seen that the α-MgAgSb/$Mg_3(Sb,Bi)_2$ prototype built by Ying *et al.* shows a higher maximum conversion efficiency for the same temperature difference[40], as it reaches a value of 8.5%. Other α-MgAgSb/$Mg_3(Sb,Bi)_2$ prototypes show higher conversion efficiencies that we obtained in this work.[39, 81, 82] Nonetheless, the n-type material is less healthy, cheap and sustainable than $Mg_2(Si,Sn)$. Moreover, tin and bismuth make up around 60% of the powder used to synthetize $Mg_2(Si,Sn)$ and $Mg_3(Bi,Sb)_2$ respectively, but tin is over 1000 times more abundant than bismuth in the Earth's crust. Magnesium is the second-heaviest fraction in both, while silicon (3. in $Mg_2(Si,Sn)$) surpasses antimony's (3. in $Mg_3(Bi,Sb)_2$) abundance by more than a million times.[83] For large scale applications where abundant materials are required and ecological compatibility is highly desirable, this might overcompensate the so far lower performance of $Mg_2(Si,Sn)$ compared to $Mg_3(Bi,Sb)_2$.A further criterion for applicability is the long-term stability. Both $Mg_3(Sb,Bi)_2$ and $Mg_2(Si,Sn)$ show a finite solubility range which affects carrier concentration and with this the material performance[61, 84, 85], however the solubility range for $Mg_3(Sb,Bi)_2$ is larger, possibly indicating that further material protection against Mg loss is required eventually. We also note that some of the mentioned works rely on scarce Te[81] for tuning the carrier concentration while this is not the case for our material combination.

Though commercial BiTe-based TEM show higher conversion efficiencies at lower temperature difference, our α-MgAgSb/$Mg_2(Si,Sn)$ prototype exhibits a similar conversion efficiency for ΔT = 225 K and is superior at higher ΔT.[86] Finally our TEM shows higher performance compared to the fully $Mg_2(Si,Sn)$-based TEM built by Camut *et al*.[47] and other low cost alternatives based *e.g.* oxides[87, 88]. Therefore, our new material combination seems a good compromise between sustainability and high performance.

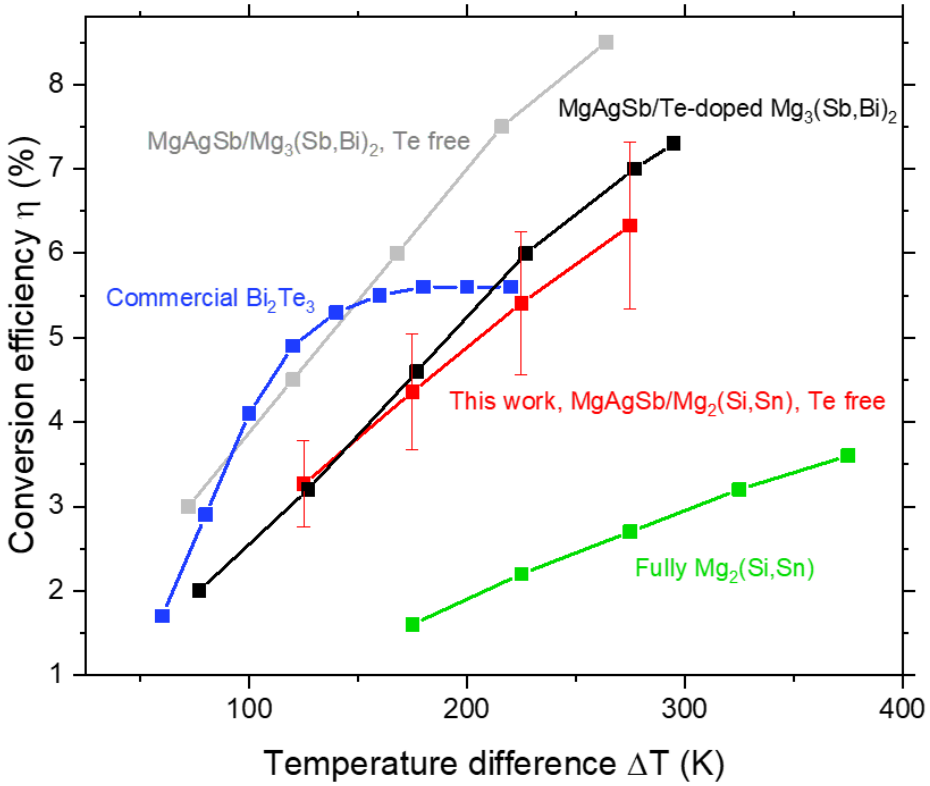

Figure 7: Conversion efficiency as a function of the temperature difference applied to the TEM for several reported TEMs. Data were taken from other studies[40, 47, 81, 86]. The error bars represent the measurement uncertainties

Conclusion

We have presented the first demonstration of an α-MgAgSb/Mg_2(Si,Sn)-based TEM. The prototype shows a maximum conversion efficiency of 6.4% and a maximum power of 0.68 W for a temperature difference of 275 K. Over the course of three measurement cycles, the TEM shows a stable performance, with small, compensating changes in internal resistance and open loop voltage. Comparison and analysis of the measurement data with the Constant Property Model showed a good match for most parameters, indicated relatively low losses due to thermal interface resistances (<10%) and indicates that maximum conversion efficiency and power of 7.5% and 0.8 W, respectively can be expected if the electrical contact resistances are reduced further. By using Mg_2(Si,Sn), we have substituted the slightly more performant, but less abundant, more toxic and less lightweight Mg_3Sb_2, which is often combined with α-MgAgSb. The relative low weight of this device makes it very attractive for aerospace applications.

Acknowledgements

The authors and the entire LUNA project team want to acknowledge the government of North Rhein Westphalia for the funds received to finance the outfitting of the LUNA facility. This work having been made possible by the Spaceship EAC Initiative, the author would also like to acknowledge the financial support provided the European Astronaut Centre as part of the European Space Agency. The author would finally like to acknowledge P. Blaschkewitz for the TEGMA measurement and C. Stiewe for his support.

References

1. Twaha, S., et al., *A comprehensive review of thermoelectric technology: Materials, applications, modelling and performance improvement.* Renewable and Sustainable Energy Reviews, 2016. **65**: p. 698-726.
2. Schierning, G., *Bring on the heat.* Nature Energy, 2018. **3**: p. 92-93.
3. Bell, L.E., *Cooling, Heating, Generating Power, and Recovering Waste Heat with Thermoelectric Systems.* Science, 2008. **321**: p. 1457-1461.
4. Goldsmid, H.J., *Introduction to Thermoelectricity*. Springer Series, ed. R. Hull. 2010, Materials Science.
5. Snyder, G. and A. Snyder, *Figure of Merit ZT of a Thermoelectric Device from Materials Properties.* Energy Environ. Sci., 2017. **10**.
6. Snyder, G.J., *Complex thermoelectric materials.* Nature materials, 2008. **7**: p. 105-114.
7. Wood, C., *Materials for thermoelectric energy conversion* Reports on Progress in Physics, 1988. **51**(459).
8. Snyder, G.J., *Small thermoelectric generators.* Electrochemical Society Interface, 2008. **17**(54).
9. LeBlanc, S., *Thermoelectric generators: Linking material properties and systems engineering for waste heat recovery applications.* Sustainable Materials and Technologies, 2014. **1-2**: p. 26-35.
10. Ebling, D.G., et al., *Development of a System for Thermoelectric Heat Recovery from Stationary Industrial Processes.* Journal of Electronic Materials, 2016. **45**(7): p. 3433-3439.
11. Weng, C.-C. and M.-J. Huang, *A simulation study of automotive waste heat recovery using a thermoelectric power generator.* International Journal of Thermal Sciences, 2013. **71**: p. 302-309.
12. Li, K., et al., *Thermoelectric power generator: Field test at Bottle Rock geothermal power plant.* Journal of Power Sources, 2021. **485**: p. 229266.
13. Wahbah, M., et al., *Characterization of human body-based thermal and vibration energy harvesting for wearable devices.* IEEE Journal on Emerging and Selected Topics in Circuits and Systems, 2014. **4**(3): p. 354-363.
14. Dilhac, J.-M., et al., *Implementation of Thermoelectric Generators in Airlinersfor Powering Battery-Free Wireless Sensor Networks.* Journal of Electronic Materials, 2014. **43**(6): p. 2444-2451.
15. Kishi, M., et al. *Micro thermoelectric modules and their application to wristwatches as an energy source*. in *Eighteenth International Conference on Thermoelectrics. Proceedings, ICT'99 (Cat. No.99TH8407)*. 1999.
16. Fisk, L.A., *Journey into the Unknown Beyond.* Science, 2005. **309**(5743): p. 2016-2017.
17. Holgate, T.C., et al., *Increasing the Efficiency of the Multi-mission Radioisotope Thermoelectric Generator.* Journal of Electronic Materials, 2015. **44**(6): p. 1814-1821.
18. Sharma, S. and U. Schwingenschlögl, *Thermoelectric Response in Single Quintuple Layer Bi2Te3.* ACS Energy Letters, 2016. **1**(4): p. 875-879.
19. Mamur, H., et al., *A review on bismuth telluride (Bi2Te3) nanostructure for thermoelectric applications.* Renewable and Sustainable Energy Reviews, 2018. **82**: p. 4159-4169.
20. Hao, F., et al., *High efficiency Bi2Te3-based materials and devices for thermoelectric power generation between 100 and 300 °C.* Energy & Environmental Science, 2016. **9**(10): p. 3120-3127.
21. Hachiuma, H., *Activities and Future Vision of Komatsu Thermo modules*, in *Proceedings of the Fifth European Conference on Thermoelectrics*. 2007: Odessa Ukraine.
22. Taylor, S.R., *Abundance of chemical elements in the continental crust: a new table.* Geochimica et Cosmochimica Acta 1964. **28**: p. 1273-1285.
23. Ashraf, W., et al., *Toxicity of tellurium and its compounds.* Physical Sciences Reviews, 2022.
24. Yu, J., et al., *Half-Heusler Thermoelectric Module with High Conversion Efficiency and High Power Density.* Advanced Energy Materials, 2020. **10**(25).
25. Chu, J., et al., *Electrode interface optimization advances conversion efficiency and stability of thermoelectric devices.* Nat Commun, 2020. **11**(1): p. 2723.
26. Rogl, G. and P. Rogl, *Skutterudites, a most promising group of thermoelectric materials.* Current Opinion in Green and Sustainable Chemistry, 2017. **4**: p. 50-57.
27. Mitra, M., et al., *Conventional Half-Heusler alloys advance state-of-the-art thermoelectric properties.* Materials Today Physics, 2022. **28**: p. 100900.
28. Kirkham, M.J., et al., *Abinitiodetermination of crystal structures of the thermoelectric material MgAgSb.* Physical Review B, 2012. **85**(14).

29. Amatya, R., *Trend for Thermoelectric Materials and Their Earth Abundance.* Journal of Electronic Materials, 2011. **41**(6): p. 1011-1019.
30. Li, G., et al., *Intrinsic mechanical behavior of MgAgSb thermoelectric material: An ab initio study.* Journal of Materiomics, 2020. **6**(1): p. 24-32.
31. Zhao, H., et al., *High thermoelectric performance of MgAgSb-based materials.* Nano Energy, 2014. **7**: p. 97-103.
32. Liu, Z., et al., *High thermoelectric performance of α-MgAgSb for power generation.* Energy & Environmental Science, 2018. **11**(1): p. 23-44.
33. Rodriguez-Barber, I., et al., *On the influence of AgMg precursor formation on MgAgSb microstructure and thermoelectric properties.* Journal of Alloys and Compounds, 2021. **860**.
34. Duparchy, A., et al., *Establishing synthesis–composition–property relationships for enhanced and reproducible thermoelectric properties of MgAgSb.* Journal of Materials Chemistry A, 2022. **10**(40): p. 21716-21726.
35. Gao, W., et al., *The critical role of boron doping in the thermoelectric and mechanical properties of nanostructured α-MgAgSb.* Journal of Materials Chemistry C, 2018. **6**(36): p. 9821-9827.
36. Liu, Z., et al., *Lithium Doping to Enhance Thermoelectric Performance of MgAgSb with Weak Electron-Phonon Coupling.* Advanced Energy Materials, 2016. **6**(7).
37. Kraemer, D., et al., *High thermoelectric conversion efficiency of MgAgSb-based material with hot-pressed contacts.* Energy & Environmental Science, 2015. **8**(4): p. 1299-1308.
38. Liu, Z., et al., *Maximizing the performance of n-type Mg3Bi2 based materials for room-temperature power generation and thermoelectric cooling.* Nature Communications, 2022. **13**(1): p. 1120.
39. Ying, P., et al., *Towards tellurium-free thermoelectric modules for power generation from low-grade heat.* Nat Commun, 2021. **12**(1): p. 1121.
40. Ying, P., et al., *A robust thermoelectric module based on MgAgSb/Mg3(Sb,Bi)2with a conversion efficiency of 8.5% and a maximum cooling of 72 K.* Energy & Environmental Science, 2022. **15**(6): p. 2557-2566.
41. Ouyang, Z. and D. Li, *Modelling of segmented high-performance thermoelectric generators with effects of thermal radiation, electrical and thermal contact resistances.* Sci Rep, 2016. **6**: p. 24123.
42. LeBlanc, S., et al., *Material and manufacturing cost considerations for thermoelectrics.* Renewable and Sustainable Energy Reviews, 2014. **32**: p. 313-327.
43. Zaitsev, V.K., et al., *Highly effectiveMg2Si1−xSnxthermoelectrics.* Physical Review B, 2006. **74**(4).
44. Farahi, N., et al., *High efficiency Mg(2)(Si,Sn)-based thermoelectric materials: scale-up synthesis, functional homogeneity, and thermal stability.* RSC Adv, 2019. **9**(40): p. 23021-23028.
45. Liu, W., et al., *Convergence of Conduction Bands as a Means of Enhancing Thermoelectric Performance of n-Type Mg2Si1-xSnx Solid Solutions.* Physical Review Letters, 2012. **108**(16): p. 166601.
46. Goyal, G.K. and T. Dasgupta, *Fabrication and testing of Mg2Si1-xSnx based thermoelectric generator module.* Materials Science and Engineering: B, 2021. **272**.
47. Camut, J., et al., *Efficiency Measurement and Modeling of a High-Performance Mg2(Si,Sn)-Based Thermoelectric Generator.* Advanced Engineering Materials, 2022. **25**(1).
48. Kamila, H., et al., *Synthesis of p-type Mg2Si1-xSnx with x = 0-1 and optimization of the synthesis parameters.* Materials Today: Proceedings, 2019. **8**: p. 546-555.
49. Gelbstein, Y., et al., *Physical, Mechanical, and Structural Properties of Highly Efficient Nanostructured n- and p-Silicides for Practical Thermoelectric Applications.* Journal of Electronic Materials, 2013. **43**(6): p. 1703-1711.
50. Ioffe, A., *Semiconductor thermoelements and thermoelectric cooling*. 1957, London, Infosearch, ltd.
51. Ponnusamy, P., J. de Boor, and E. Muller, *Discrepancy between Constant Properties Model and Temperature-Dependent Material Properties for Performance Estimation of Thermoelectric Generators.* Entropy (Basel), 2020. **22**(10).
52. Ayachi, S., *Developing Contacting Solutions for Mg2Si1-xSnx-based Thermoelectric Generators: Cu and Ni45Cu55 as Potential Contacting Electrodes* ACS applied materials & interfaces, 2019. **11**(40769).
53. Camut, J., et al., *Overcoming Asymmetric Contact Resistances in Al-Contacted Mg2(Si,Sn) Thermoelectric Legs.* Materials, 2021. **14**(22).
54. Ziolkowski, P., et al., *Probing thermopower on the microscale.* physica status solidi (a), 2013. **210**(1): p. 89-105.

55. Camut, J., et al., *Aluminum as promising electrode for Mg2(Si,Sn)-based thermoelectric devices.* Materials Today Energy, 2021. **21**.
56. de Boor, J., et al., *Fabrication and characterization of nickel contacts for magnesium silicide based thermoelectric generators.* Journal of Alloys and Compounds, 2015. **632**: p. 348-353.
57. Bjørk, R., *The Universal Influence of Contact Resistance on the Efficiency of a Thermoelectric Generator.* Journal of Electronic Materials, 2015. **44**(8): p. 2869-2876.
58. Erturun, U., K. Erermis, and K. Mossi, *Influence of leg sizing and spacing on power generation and thermal stresses of thermoelectric devices.* Applied Energy, 2015. **159**: p. 19-27.
59. Ziolkowski, P., P. Blaschkewitz, and E. Müller, *Heat flow measurement as a key to standardization of thermoelectric generator module metrology: A comparison of reference and absolute techniques.* Measurement, 2021. **167**.
60. Ziolkowski, P., P. Blaschkewitz, and E. Müller, *Validation of commercial Bi2Te3-based thermoelectric generator modules for application as metrological reference samples.* Measurement, 2021. **177**.
61. Sankhla, A., et al., *On the role of Mg content in Mg2(Si,Sn): Assessing its impact on electronic transport and estimating the phase width by in situ characterization and modelling.* Materials Today Physics, 2021. **21**: p. 100471.
62. Ziolkowski, P., et al., *International Round Robin Test of Thermoelectric Generator Modules.* Materials (Basel), 2022. **15**(5).
63. Armstrong, H., et al., *Estimating Energy Conversion Efficiency of Thermoelectric Materials: Constant Property Versus Average Property Models.* Journal of Electronic Materials, 2016. **46**(1): p. 6-13.
64. Zhang, M., et al., *Influence of Thomson effect on the thermoelectric generator.* International Journal of Heat and Mass Transfer, 2019. **137**: p. 1183-1190.
65. Huang, M.-J., R.-H. Yen, and A.-B. Wang, *The influence of the Thomson effect on the performance of a thermoelectric cooler.* International Journal of Heat and Mass Transfer, 2005. **48**(2): p. 413-418.
66. Ponnusamy, P., J. de Boor, and E. Müller, *Using the constant properties model for accurate performance estimation of thermoelectric generator elements.* Applied Energy, 2020. **262**.
67. de Boor, J., et al., *High-Temperature Measurement of Seebeck Coefficient and Electrical Conductivity.* Journal of Electronic Materials, 2013. **42**(7): p. 1711-1718.
68. Borup, K.A., et al., *Measuring thermoelectric transport properties of materials.* Energy & Environmental Science, 2015. **8**(2): p. 423-435.
69. May, A.F. and G.J. Snyder. *Introduction to Modeling Thermoelectric Transport at High Temperatures*. 2012.
70. Camut, J., E. Müller, and J. de Boor, *Analyzing the Performance of Thermoelectric Generators with Inhomogeneous Legs: Coupled Material–Device Modelling for Mg2X-Based TEG Prototypes.* Energies, 2023. **16**(9).
71. Yang, P., et al., *Analysis of Peak Electromagnetic Torque Characteristics for Superconducting DC Induction Heaters.* IEEE Access, 2020. **8**: p. 14777-14788.
72. Apertet, Y., et al., *Optimal working conditions for thermoelectric generators with realistic thermal coupling.* Europhysics Letters, 2012. **97**(2): p. 28001.
73. Yin, L., et al., *Low-temperature sintering of Ag nanoparticles for high-performance thermoelectric module design.* Nature Energy, 2023.
74. Camut, J., *Development of Mg_2(Si,Sn)-based thermoelectric generators: investigating contacting solutions, fabrication process, evaluating measurement reliability and optimization paths via modelling*. 2023, Duisburg-Essen University.
75. Skomedal, G., et al., *Design, assembly and characterization of silicide-based thermoelectric modules.* Energy Conversion and Management, 2016. **110**: p. 13-21.
76. Mejri, M., *Characterization of the thermo-mechanical properties of p-type (MnSi1.77) and n-type (Mg2Si0.6Sn0.4) thermoelectric materials.* Scripta Materialia, 2019. **172**(28).
77. Kaibe, H.T., et al., *Development of thermoelectric generating stacked modules aiming for 15% of conversion efficiency.* ICT 2005. 24th International Conference on Thermoelectrics, 2005., 2005: p. 242-247.
78. Barako, M.T., et al. *A reliability study with infrared imaging of thermoelectric modules under thermal cycling*. in *13th InterSociety Conference on Thermal and Thermomechanical Phenomena in Electronic Systems*. 2012.

79. Greenhall, J., et al., *Nonlinear acoustic crack detection in thermoelectric wafers.* Mechanical Systems and Signal Processing, 2020. **139**: p. 106598.
80. Ponnusamy, P., *Critical analysis of a Constant Properties Model for performance analysis of thermoelectric generators*. 2022, Duisburg-Essen.
81. Liu, Z., et al., *Demonstration of ultrahigh thermoelectric efficiency of ~7.3% in Mg3Sb2/MgAgSb module for low-temperature energy harvesting.* Joule, 2021. **5**(5): p. 1196-1208.
82. Jiang, M., et al., *High-efficiency and reliable same-parent thermoelectric modules using Mg3Sb2-based compounds.* National Science Review, 2023. **10**(6).
83. *Abundance of elements in the earth's crust and in the sea*. 97th ed. 2016-2017, p. 14-17, CRC Handbook of Chemistry and Physics.
84. Ohno, S., et al., *Phase Boundary Mapping to Obtain n-type Mg3Sb2-Based Thermoelectrics.* Joule, 2018. **2**(1): p. 141-154.
85. Kato, D. and K. Iwasaki, *Mg-pressure-controlled annealing for tuning Mg content and thermoelectric properties of Mg2–δ(Si0.5Sn0.5)1–xSbx.* Journal of Alloys and Compounds, 2021. **856**: p. 157351.
86. Nozariasbmarz, A., et al., *Bismuth Telluride Thermoelectrics with 8% Module Efficiency for Waste Heat Recovery Application.* iScience, 2020. **23**(7): p. 101340.
87. Funahashi, R., et al., *Power Generation Using Oxide Thermoelectric Modules*, in *Mass and Charge Transport in Inorganic Materials III*. 2006. p. 158-167.
88. Funahashi, R., et al., *High-throughput screening of thermoelectric oxides and power generation modules consisting of oxide unicouples.* Measurement Science and Technology, 2005. **16**(1): p. 70.